Università Cattolica del Sacro Cuore

Sede di Brescia

Facoltà di Scienze Matematiche, Fisiche e Naturali

Corso di Laurea Specialistica in Fisica

Tesi di Laurea

Fabrication and time-resolved optical investigation of hypersonic phononic crystals

Relatore:

Dott. Francesco Banfi

Correlatore:

Dott. Pasqualantonio Pingue

Laureando: **Marco Travagliati**

mat. 3611045

Anno Accademico 2008/2009

Acknowledgments

I would like to thank my advisors Francesco and Pasquale who let me live this great adventure and made it very pleasant. I am deeply indebted to Damiano who ~~have~~ assisted me constantly in Brescia. I have learnt a great deal from Franco, Daniele, Elia, Marco and Vincenzo and I gratefully acknowledge my debt to them. I wish also thank all the other people working in Laboratorio NEST, especially Lorenzo, Ang, Fabio and Simone, who made me feel like home also when I was in Pisa.

A special thanks goes to all the people of the ELPHOS Lab who helped and guided me in these years at the University and whose friendship meant a great deal to me.

Contents

Chapter 1

Introduction

1.1 Overview

The scientific and technological interest in the field of thermomechanics at the nanoscale grew at a tremendous pace in the last decade, thanks to the availability of novel material processing and growth techniques, and to the emergence of new detection methods.

In nanostructured systems the thermomechanical dynamics takes places on a time scale ranging from few picoseconds to tens of nanosecond, and on sub-μm length scales. These scales question the applicability of theoretical frames so far applied to bulk systems and call for experiments providing fast-time resolution and low-perturbing sensitive probes.

Under an applicative standpoint, issues such as thermal management in nanoelectronic devices, thermomechanical responses in MicroElectroMechanical Systems (MEMS) and Opto-Acoustical devices in the hypersonic frequency range for high resolution imaging or mass trafficking, just to mention a few, are of paramount importance [1, 2, 3, 4, 5, 6].

Surface-based phononic crystals emerge as particularly suited toy systems to access, in conjunction with time-resolved ultrafast optics, both thermal and me-

chanical properties of nanosystems. ~~They~~ are periodic elastic composites of two or more vibrating materials, obtained patterning the surface of a substrate material either by metal deposition or substrate etching.

All-optical time-resolved experiments on a periodic optical lattice, like a surface-based phononic crystal, allow to deliver an energy density δU_V to the nanostructure and to follow, in the time domain, energy relaxation process from the nanostructure to the substrate [7], ~~that serves~~ as an external thermal bath. In these experiments both the thermal δQ_V, and mechanical energy δW_V, [8, 9], branching from the absorbed total energy δU_V, can be traced. The optical probe (besides providing the required time-resolution) is a non-contact low-perturbing one: this peculiarity is particularly important for detection of minute thermal fluxes and displacements fields.

The present work stems from this context. We fabricated surface-based phononic crystals ~~composed by~~ aluminum disks of nanometric size arranged in a square lattice on the surface of a silicon substrate ~~and~~ we investigated ~~their~~ thermomechanical dynamics by time-resolved optical diffraction measurements. Previous measurements did not allow for a clear understanding of the thermal dynamics, the problem arising from the mechanical and thermal dynamics occurring on the same time scale. We explored strategies to overcome the above-mentioned drawback, either by decoupling the two time scales or by quenching the mechanical dynamics.

As far as the thermal problem is involved, the ideal experimental situation would be using a transparent (that is optically non-absorbing) substrate. This is especially desirable when the laser repetition rate falls in the 10 KHz range or below [8]. For this reasons we also attempted replacing the Si substrate with a glass one. With this aim in mind we explored a new fabrication technique for this kind of samples.

1.2   Outline

This work is organized as follows. In Chapter 2 we present in brief ~~a theoretical~~ ~~picture of~~ the behavior of a phononic crystal under ~~an~~ impulsive laser irradiation: we describe the acoustic eigenmodes of the system, which of them are excited and we introduce a simple analytical model allowing to grasp the physics behind the thermal relaxation process. In Chapter 3 ~~after a~~ review of the basics of time-resolved optical diffraction experiments~~,~~ we analyze two strategies, on which the sample design were based, to decouple the time scales of these thermal and mechanical dynamics. The sample fabrication process is described in Chapter 4. In Chapter 5 we illustrate the experimental setup for time-resolved optical diffraction experiments and we discuss the results of our measu   . The novel fabrication process of samples based on glass substrates, ~~and the~~ results of preliminary measurements on these samples, are reported in appendix A.

Chapter 2

Thermomechanics of hypersonic phononic crystals in brief

In this chapter we start presenting a theoretical investigation on the nature of the acoustic eigenmodes of a surface phononic crystal. Attention is then devoted on the sample's excitation mechanism and in spotting out the excited mechanical eigenmodes. A simple analytical model, allowing to understand, by means of few parameters, the basic thermal dynamics of the system under investigation, is explained in Section 2.2. These tools provide the basic understanding to foresee possible experimental strategies to decouple the thermal and mechanical time scales.

2.1   Pseudosurface acoustic modes in a phononic crystal and their optical excitation

The mechanical behavior of phononic crystals is well described in the framework of continuum mechanics. In this work only the linear elastic regime will be considered, unless otherwise stated. In this context the evolution of the system is described by the Navier equation, that in an homogeneous and isotropic medium reads

$$\rho\ddot{\mathbf{u}} = (\lambda + \mu)\nabla(\nabla \cdot \mathbf{u}) + \mu\nabla^2\mathbf{u}, \tag{2.1}$$

where $\mathbf{u}$ is the displacement field, ρ the mass density of the medium, and λ and μ are its Lamè constants. For an harmonic time dependence $e^{i\omega t} + c.c.$ of the displacement field $\mathbf{u}$, one obtains the eigenvalue equation

$$-\rho\omega^2\mathbf{u} = (\lambda + \mu)\nabla(\nabla \cdot \mathbf{u}) + \mu\nabla^2\mathbf{u}, \tag{2.2}$$

$\mathbf{u}$ being the eigenmode corresponding to frequency ω.

In an infinite medium the eigenmodes are either transverse or longitudinally polarized. The longitudinal modes imply non zero compression and rarefaction of the solid as the displacement is parallel to the wavevector, as seen in Fig. 2.1(a). In the transverse modes, that are twofold degenerate, the displacement is perpendicular to the wavevector so there's no change in the density of the solid, but a shear stress sets in, as seen in Fig. 2.1(b). The transverse and longitudinal polarized eigenmodes have different velocity, c_t and c_l respectively, with $c_l > c_t$.

In a semi-infinite medium the full translational symmetry is broken thus allowing for a new kind of eigenmodes: the surface acoustic waves (SAWs), also called Rayleigh waves. These waves travel along the interface confined within a wavelength from the surface. SAWs have both longitudinal and shear vertical components, and their displacement field is in the plane formed by the wavevector and the normal to the interface. Surface acoustic waves are 'circularly polarized', being the longitudinal and shear vertical components out of phase by $\pi/2$, as shown in
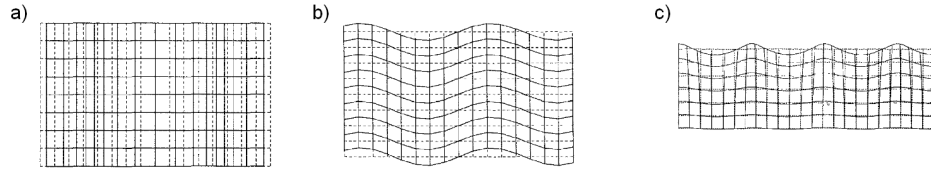
FIGURE 2.1: Displacement field for (a) longitudinal mode, (b) transverse mode and (c) SAW. The former two modes are bulk ones, while the latter is confined within a wavelength from the surface [11].

Fig. 2.1(c). The relation between the velocities of these three kinds of waves is $c_l > c_t > c_{SAW}$, c_{SAW} being the SAW velocity [10].

A periodic structure deposited on the substrate surface, like the ordered array of metallic nanodisks investigated in the present work, changes the eigenvalue problem:

- the Bloch theorem applies, it is possible to define a reduced wavevector, and the solution are found solving the eigenvalue equation in a primitive cell imposing Bloch boundary conditions;

- from a perturbative point of view, the periodic overlayer can be seen as a scatterer for the otherwise unperturbed substrate eigenmodes.

In the reduced zone scheme, for each reduced wavevector there are infinite modes with different frequencies. This is pictured in Fig. 2.2, where the projected phonon dispersion is schematically reported. In a semi-infinite crystal, that is neglecting the scattering centers, the Bloch modes have a twofold degeneracy both at the edges and at center of the Brillouin zone. The degenerate modes have different symmetries of the displacement field: the cos-like (gerade) and sin-like (ungerade) symmetries.

The periodic overlayer couples the SAW modes to the bulk ones therefore the SAWs are not eigenmodes when the overlayer is added. The eigenmodes of the surface phononic crystal reminiscent of the SAWs are addressed as pseudo-SAWs [13]. In these modes the majority of the mechanical energy lies in the periodic
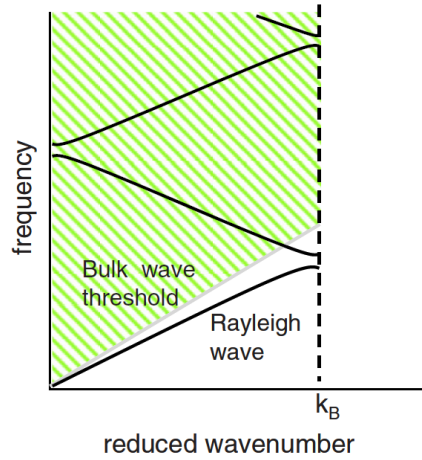
FIGURE 2.2: Schematic representation of acoustic band dispersion in a planar phononic crystal [12].

overlayer and within a wavelength underneath the interface (similarly to a SAW in semi-infinite crystal slab), but there's also an energy content irradiated into the bulk (in contrast with a SAW in a semi-infinite slab), as reported in Fig. 2.3.

This thesis will focus on pseudo-SAW modes. The periodic overlayer removes the pseudo-SAW degeneracy both at the center and at the edges of the Brillouin zone. The periodicity is responsible for the frequency gap opening at the above mentioned points of the Brillouin zone. This is similar to what occurs in electronic or phononic band structures [14].

In the experiments that are reported here, an 800 nm wavelength - 150 fs duration laser pulse strikes the phononic crystal. The energy density absorbed by the sample δU_V is peaked within the nanodisks, leaving the substrate temperature unaltered. This selectivity is possible because of the difference in the optical penetration depths between aluminum and silicon, respectively the nanodisks and substrate material. The increase of the temperature of the periodic metallic nanodisks triggers a spatially modulated stress on the silicon surface. Such stress launches a pseudo-SAW of wavelength λ matching the nanodisks lattice periodicity $p = 1\ \mu$m. The launching process symmetry, i.e. the laser spot impinging on
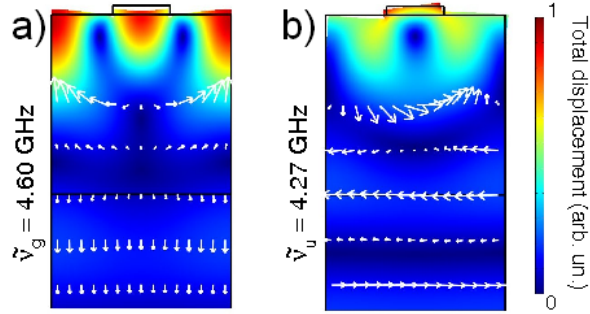
FIGURE 2.3: Displacement field in the top 2 μm portion of the unit cell of a surface phononic crystal as obtained from Finite Element Method-based calculations. The deformation and arrows correspond to the displacement field, while the color scale refers to the normalized total displacement. Cos-like (gerade) (a) and sin-like (ungerade) (b) pseudo-SAW solutions of a stripe of width $w = 320$ nm. The two pseudo-SAW eigenfrequencies are $\nu_g = 4.60$ GHz and $\nu_u = 4.27$ GHz [13].

the surface phononic crystal, is radial symmetric, hence only cos-like pseudo-SAWs are excited [8].

The nanodisks lattice is oriented along the Si(100) direction, which we take as the x-axis in our reference system. The wavevectors are labeled as $K_{x,n} = k_x + 2\pi n/\lambda$, k_x varying in the range $(-\pi/\lambda, \pi/\lambda)$. In the present work the excited wavevector has $n = 1$ and $k_x = 0$, that is $K_{x,1} = 2\pi/\lambda$, corresponding to the first harmonic, also called the fundamental, at the center of the surface Brillouin zone [13]. The SAW wave velocity along Si(100) is $c_{SAW} \sim 5000$ m/s [15], thus yielding a frequency of the excited pseudo-SAW mode $\nu \sim c_{SAW} \frac{K_{x,1}}{2\pi} \sim 5$ GHz, in the hypersonic range.

2.2   Thermal dynamics of a thin film under impulsive heating

The thermal behavior of the sample under the irradiation of an ultrashort laser pulse involves three different processes on well separated time scales.

1. The heating of electrons inside the nanodisks under the absorption of a single pulse (sub-ps timescale).

2. The thermalization of electrons and phonons inside the nanodisks. The temperature mismatch ΔT between the nanodisk and the silicon substrate triggers an impulsive expansion of the nanostructures diameters ($\delta d/d \sim \alpha^* \Delta T$, α^* being the effective thermal expansion coefficient of the Al/Si system). The expansion is responsible for the excitation of the acoustic modes (ps timescale).

3. The energy relaxation of the nanodisk to the substrate. In this step the energy density δU_V absorbed from the laser pulse is delivered to the substrate via a mechanical channel, δW_V (pseudo-SAW), and a thermal one, δQ_V. The heat flux dominates over the mechanical one: following [7], we have $\delta Q_V / \delta W_V \sim 10^{-5}$ [16].

In our experiments the above mentioned three step process repeats itself upon arrival of the following laser pump pulse, that it every $2\pi/\omega_{rep}$, ω_{rep} being the laser repetition rate. We are interested in the investigation of the thermal problem taking place in the third step.

The conservation of energy imposes that

$$-\nabla \cdot \mathbf{q} + g(\mathbf{r}, t) = \rho c_m \frac{\partial T}{\partial t}$$

where $g(\mathbf{r}, t)$ is the power density source term (W/m^3), $-\nabla \cdot \mathbf{q}$ is the power density sink (W/m^3), $\mathbf{q}$ being the heat flux (W/m^2), and $\rho c_m \partial T/\partial t$ is the instantaneous
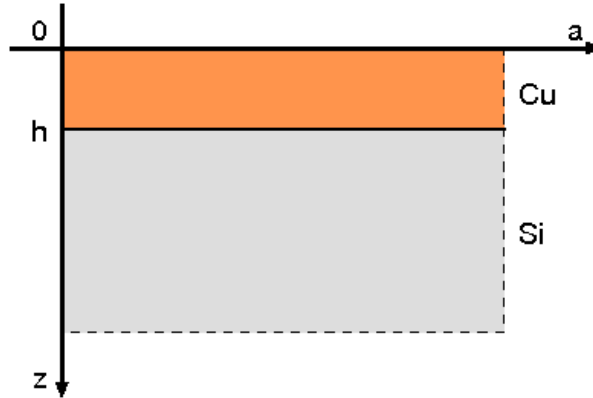
FIGURE 2.4: Geometry of the metal film deposited on a substrate, adopted in the analytical solution of the 1D thermal evolution problem [18].

power density (ρ is the mass density and c_m the specific heat capacity for unit of mass). Let's assume that the constitutive equation for the heat flux is the Fourier equation

$$\mathbf{q} = -\kappa \nabla T.$$

The conservation equation then reads:

$$\kappa \nabla^2 T + g(\mathbf{r}, t) = \rho c_m \frac{\partial T}{\partial t}. \tag{2.3}$$

In our problem the source term accounts for laser energy absorption. If we consider the high thermal conductivity of aluminum ($\kappa_{Al} = 327$ Wm^{-1}K^{-1} [17]), the penetration depth of the 800 nm laser light in it ($\Lambda_{Al} = 7$ nm [17]) and the disks thickness (maximum 85 nm in our samples), we can assume that after the electron-phonon thermalization (few picoseconds) the disk is isothermal at a temperature $T_0 \sim 305$ K [16]. In this way it's possible solve the problem described by Eq. 2.3 without the source term and accounting for it through the initial temperature condition T_0 in the disk. The absorption of the laser energy by the silicon substrate is assumed negligible. The silicon substrate is taken as a thermal reservoir at constant temperature T_{sub}.

For simplicity let's consider the film geometry in Fig. 2.4 as mimicking the nanodisk. This simplification reduces the thermal transfer to a 1D-problem thus

allowing for an analytical solution. At the film-substrate interface the heat transfer is controlled by the thermal boundary resistance ρ_{th} (m^{2}K/W) through the equation

$$\kappa \frac{\partial T}{\partial z} = \frac{1}{\rho_{th}}[T(t) - T_{sub}].$$

Assuming no heat is delivered to the air through the film surface, the following boundary condition applies at the film-air interface:

$$\frac{\partial T}{\partial z} = 0.$$

The thermal problem then has the following analytical solution [19]

$$T(z,t) = T_0 \sum_{m=1}^{\infty} \exp\left(-\frac{D}{h^2}\xi_m^2 t\right) \frac{2B}{h(\xi_m^2 + B^2) + B} \frac{\cos\left(\frac{\xi_m}{h}z\right)}{\cos \xi_m}$$

where

$$D = \frac{\kappa}{\rho c}$$

is the thermal diffusivity,

$$B = \frac{h}{\kappa \rho_{th}}$$

is the Biot number and ξ_m are the roots of the equation

$$\xi_m \tan \xi_m = B.$$

If $B \ll 1$ the terms with $m > 1$ can be neglected and we have a single exponential decay of the temperature with a decay constant

$$\tau_{th} = (\rho c_m \rho_{th}) h. \tag{2.4}$$

$B \ll 1$ also implies that the temperature difference across the film thickness is negligible and the film can be considered isothermal during the entire thermalization process.

The thermal boundary resistance (not to be confused with thermal resistivity) of a metal on silicon is on the order of 10^{-8} m^{2}K/W, hence we estimate for our disks thickness (20 nm$< h <$85 nm) $B \sim 0.05$, that is the approximation $B \ll 1$ holds

thus we expect to observe a single exponential thermal relaxation process with a decay time $\tau_{th} \sim 1$ ns (at room temperature aluminum mass density $\rho = 2700$ Kg/m^3, aluminum specific heat capacity per unit mass $c_m = 897$ JK^{-1}Kg^{-1} [17]).

Chapter 3

Decoupling the thermal and mechanical time scales

In this chapter we illlustrate the basics of time-resolved optical diffraction experiments (Section 3.1). This technique allows to follow the thermomechanical relaxation of surface-based phononic crystal, but, if the characteristic time of the mechanical dynamics is nearly equal to the thermal relaxation time, it's difficult to have a clear understanding of the thermal process, as found in previous measurements. In Section 3.2 we present the two strategies that we adopt to overcome this issue.

3.1 Principles of time-resolved optical diffraction

We adopted a pump and probe optical diffraction technique [8, 20] to investigate the thermomechanics of surface-based phononic crystals. The scheme of this experiment is reported in Fig. 3.1. An intense ultrashort laser pulse (pump) is used to excite the system, inducing a variation in its optical properties that is detected
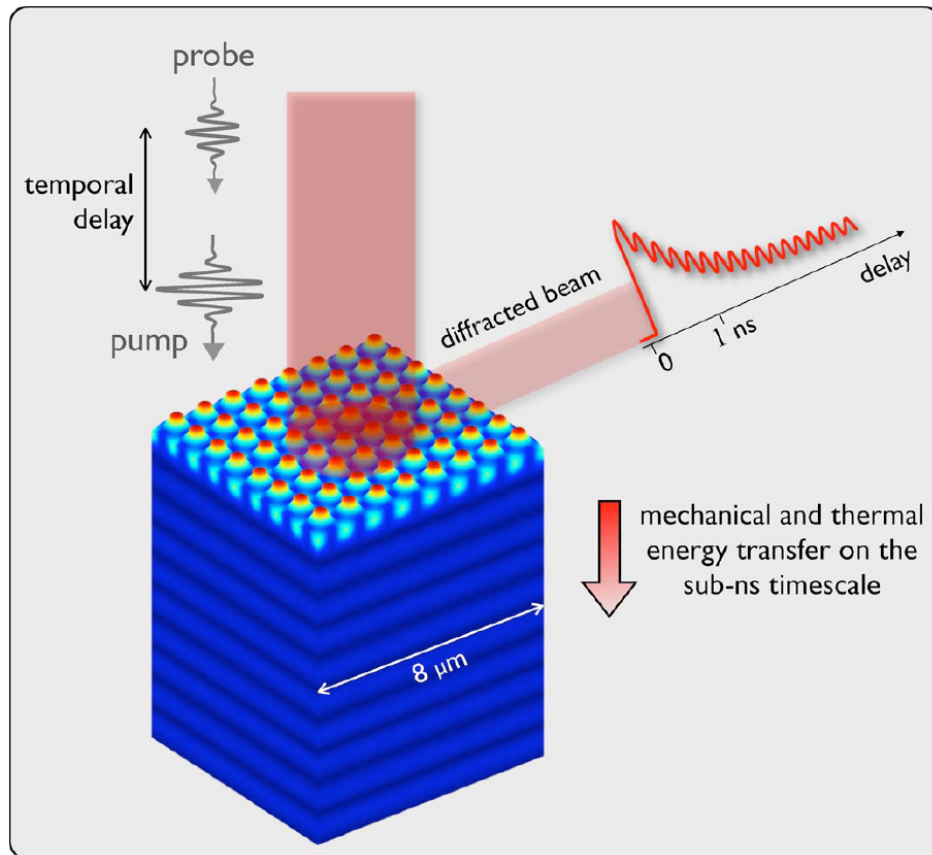
FIGURE 3.1: Schematic diagram of the experimental diffraction technique implemented to generate and detect thermomechanical transients in hypersonic surface phononic crystals [21].

analyzing the intensity of the first diffraction spot of a second ultrashort laser pulse (probe). When the probe pulse impinges on the sample after a time Δt from the pump pulse arrival, the measured intensity variation can be associated to the state of the system in the relaxation process after a time Δt from the excitation if the pulses duration is very short compared to Δt. Since we are interested in the study of a thermal relaxation process that occurs on the nanosecond time scale (see Section 2.2), we need to follow the dynamics with a resolution in the tens of picosecond range and so it's necessary to use a laser source with a sub-picosecond pulse duration. Using a laser source of this kind, scanning the delay Δt between

the pump and probe pulses, and measuring the intensity of the diffracted probe spot for each delay, we are able to follow the time evolution of the system in the relaxation process.

It has been shown [8] that the main variation in the optical constants of the system in this kind of experiments is due to the lattice expansion of the overlayer. In our case, this corresponds to a relative variation of the nanodisks radius a of the order of 10^{-5}. In principle it's possible to perform the same analysis also on the reflected or transmitted probe spot, but it has been shown that there's a signal to noise ratio enhancement if the measurement is performed in diffraction [8]. This is the reason why, even for the study of the thermal relaxation of a single nanodisk, it's suitable to deposit the nano-object in an ordered array geometry, with a periodicity that matches the central wavelength of the laser probe.

3.2   Decoupling the thermal and mechanical dynamics

As shown in the Chapter 2, the relative variation of the nanodisks diameter probes two different physical processes occurring in the phononic crystal: the thermal relaxation of the heated nanostructures toward the substrate and the surface acoustic oscillations. As described in Section 2.2, we expect that the disks radius decreases toward the equilibrium value in an exponential manner. On the same timescale pseudosurface acoustic wave are excited in the system, driving the disk radius in oscillation around its instantaneous thermal equilibrium position [9]. In this frame there are three main parameters that characterize our measured signal:

1. the thermal decay time τ_{th}, that can be estimated in terms of Eq. 2.4;

2. the frequency of the pseudo-SAW mode ν_{SAW};

3. the lifetime of the pseudo-SAW mode τ_{SAW}.
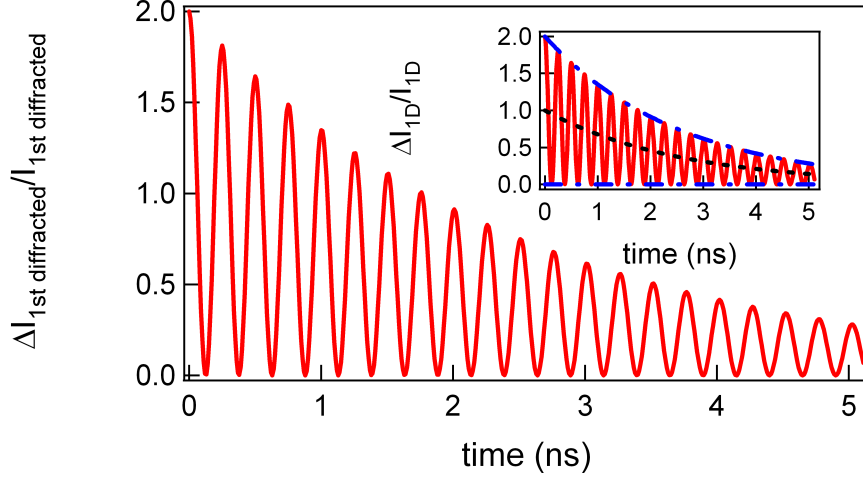
FIGURE 3.2: Expected signal in time-resolved diffraction measurement when $\tau_{th} \sim \tau_{SAW}$. In the inset the thermal decay term (black line) and the SAW damping term (blue line) of the signal are reported as a guide to the eye.

When the thermal and mechanical time scales are coupled, that is $\tau_{th} \sim \tau_{SAW}$, the relative variation of the diffracted intensity in a time-resolved optical experiment can be like the one sketched out in Fig. 3.2: in this case the oscillations due to the excited pseudo-SAW shadow the thermal decay and make difficult a precise analysis of the thermal relaxation. Our aim is to find a way to decouple these two dynamics, allowing a clear investigation of the thermal and mechanical problems by means of this experimental technique.

In the following of the section we describe two strategies that we applied to disentangle the two dynamics.

3.2.1   Strategy 1: Decoupling the time scales

Here we analyze what influences the pseudo-SAW lifetime of a surface-based phononic crystal to single out the parameters of the system that could make the mechanical time scale, τ_{SAW}, and the thermal one, τ_{th}, decoupled. The pseudo-SAW lifetime in an hypersonic surface-based phononic crystal depends on the filling fraction
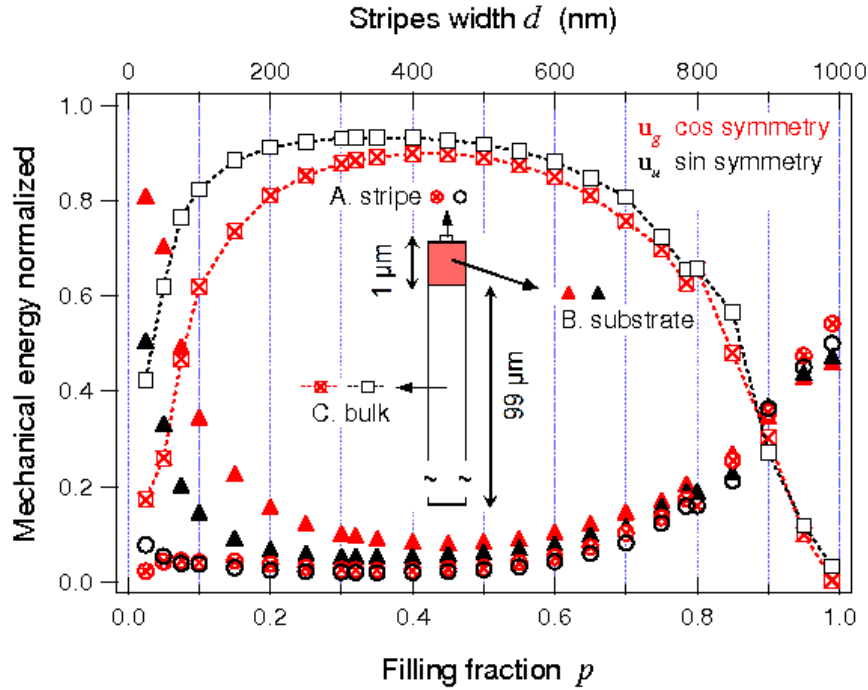
FIGURE 3.3: Analysis of the spatial distribution of the mechanical energy, normalized against the total energy inside the cell, as a function of the filling fraction for the fundamental pseudo-SAW mode in a phononic crystal made of Ni stripes deposited on a Si substrate with a periodicity of 1 μm. In the inset of this graph the region A is the stripe, the region B is the silicon within 1μm from the interface and the C region is the remaining part of the substrate [13].

of the phononic crystal, on the pseudo-SAW wavelength and on the mass of the nanodisks [13].

In Fig. 3.3 it is reported how the calculated spatial distribution of the elastic energy content (normalized against the total energy inside a cell) for the cos-like and sin-like fundamental pseudo-SAW modes varies as a function of the filling fraction. The amount of mechanical energy confined in the nanostructure and in the surface layer of the substrate (within a wavelength from the interface) is directly related to the duration of the surface oscillations: the greater this amount, the longer the lifetime of the surface oscillations. We can therefore analyze the

dependence on the filling fraction of the pseudo-SAW lifetime following these results. For a filling fraction equal to zero, that is the case of a pure silicon slab, an unperturbed SAW solution of the acoustic problem is defined. This has the entire elastic energy content localized within the interface, hence τ_{SAW} is infinite. A nanodisks array deposited on the silicon substrate acts as a scattering center coupling the SAW with the bulk modes of the system. For small filling fraction (less than 0.1), there is a weak coupling between the surface and bulk modes, with only a small amount of elastic energy radiated into the bulk, therefore the fundamental pseudo-SAW mode has a long lifetime (nanosecond time scale). On the other hand, when the substrate surface is entirely covered by a thin film, it's again defined an exact SAW solution of the acoustic problem with infinite lifetime. In this case the displacement field is waveguided at the substrate-overlayer interface. A periodic overlayer with an high filling fraction (greater than 0.8) can be regarded as a continuous film in which small holes are drilled and this situation can be described as the small filling fraction case, translating the disks into the holes, hence, even for an high filling fraction geometry, the fundamental pseudo-SAW mode has a long lifetime.

Concerning the pseudo-SAW lifetime dependence on the wavelength, it has to be noted that the shorter is the pseudo-SAW wavelength, the higher is the confinement of this mode within the surface: this implies an higher sensitivity to the presence of an overlayer. For this reason the nanostructure will scatter more effectively the mechanical energy of higher frequency modes into the bulk: the shorter the pseudo-SAW wavelength, the shorter its lifetime. This is another reason for which we can neglect in a first approximation the presence of higher harmonics of the $k = 0$ cos-like fundamental pseudo-SAW in our data: they have a sub-nanosecond lifetime.

The pseudo-SAW lifetime is also affected by the mass of the nanostructure: the lighter is the nanostructure, the longer will be the pseudo-SAW lifetime. A simple argument to grasp the origin of this dependence is the following: a surface

acoustic wave that is coupled in the same manner to an heavy nanodisk or to a light one will drive more easily into oscillation the light nanodisk because it has a lower mechanical inertia. Hence the amount of mechanical energy scattered from the surface into the bulk and the lifetime of pseudo-SAW directly depend on the mass of the nanostructure.

These considerations suggest that a proper choice of the filling fraction geometry of the overlayer can lead to the situation in which $\tau_{SAW} \gg \tau_{th}$, therefore decoupling the mechanical and thermal time scales. To test this hypothesis, we fabricated a set of samples in which the overlayer has a small filling fraction, near 0.1. The nanodisks were made of aluminum:

- aluminum is commonly used in the heat sinks that remove the unwanted heat from electronic devices, so it's interesting to investigate which is the heat transport between aluminum and silicon when the aluminum is nanostructured;

- aluminum is a light metal, this leading to a further increase of τ_{SAW}.

3.2.2   Strategy 2: Quenching the SAW

The strategy addressed in the previous section proved successful (see Section 5.2), nevertheless it serves as a proof of principle. The decoupling of the thermal and mechanical time scales was obtained by choosing aluminum (that is the metal with smaller density apart magnesium) and a filling factor of 0.1. An alternative strategy, not relying on such a peculiar metal for the nanodisks, would be desirable, and a quenching one is here proposed and investigated.

The idea consists in coating the phononic crystal with an optically transparent, thermal insulating overlayer diminishing the overall contribution of the pseudo-SAW to the diffracted optical signal. The former requirement allows applying the optical diffraction technique, whereas the latter guarantees the thermal dynamics is not altered in comparison with the uncoated phononic crystal case.

We chose polydimethylsiloxane (PDMS) rubber for the fabrication of this over-layer. This material is transparent in the visible and in the near infrared and it has a low thermal conductivity ($\kappa \sim 0.17$ W m/K, [22]), thus satisfying all of the above-mentioned requirements.

The coating layer can be expected to reduce the overall contribution of the pseudo-SAW to the diffracted optical signal either because of mass-loading effect or because the mechanical energy delivered to the systems is branched both in the silicon pseudo-SAW and in waves launched in the PDMS. The latter effect reduces the spectral weight of the pseudo-SAW and basically distributes the mechanical energy from one mode over several ones. Furthermore, due to viscoelastic effects, the modes excited in PDMS should have a fast decay time, thus subtracting energy from the mechanical modes shadowing the nanodisk-substrate thermal relaxation dynamics.

Chapter 4

Nanofabrication

In Section 4.1 we give a brief description of the fabrication process of the aluminum nanodisks lattice on silicon substrate and the recipe that we have employed. In Section 4.2 we report the characteristics of the sample that we produced. All the fabrication process was done in the cleanroom of Laboratorio NEST in Pisa.

4.1   Electron beam lithography

We fabricated our samples by electron beam lithography and lift-off. In short this fabrication procedure, as it is summarized in Fig. 4.1, was the following.

1. A substrate of proper dimension was cleaved from a wafer. The surface on which the periodic overlayer would be deposited was cleaned and then it was coated with a temporary layer of a positive e-beam resist. A positive e-beam resist is a material whose solubility in a solvent called developer results increased if it is exposed to an electron beam.

2. An electron beam was scanned across the resist surface in a pattern that was the array of circles that had the same periodicity and diameter of the disks that we had to deposit (electron beam lithography, in short EBL).
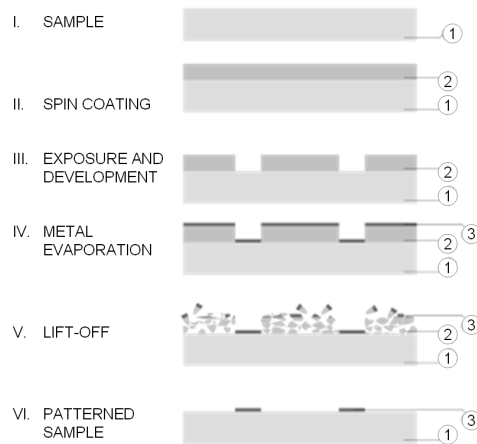
FIGURE 4.1: This is the diagram of the fundamental steps involved in the EBL
and lift-off nanofabrication process. In this image the substrate is indicated by
number 1, the resist layer by 2 and the metallic film by 3.

3. The sample was put in the developer solution for the time necessary to
   remove only the exposed area of the resist (development). The resist then
   was gently etched with a plasma oxygen to remove only the residual bumps
   of resist that were left on the substrate in the exposed area (descum).

4. On the sample surface it was deposited a film of aluminum with the same
   thickness of the nanodisks that we had to fabricate.

5. The sample was put in a resist solvent. The metallic film deposited on
   the resist surface was washed out with it, leaving only the metal deposited
   directly on the substrate. Therefore, it was obtained the desired array of
   nanodisks just in the area that was exposed to the electron beam.

In the following of this section we give the detailed recipe.

Step 1: the resist layer deposition

The resist material that we employed was poly-methyl methacrylate (PMMA)
with a 950K molecular weight. To coat the sample with a layer of this material,

we deposited on the substrate a drop of a liquid solution in which the resist was dissolved ('*Allresist AR-P 679.02*') and we spun the sample with a fixed angular velocity (4000 rpm). For a certain resist solution and substrate, the thickness of the layer depends only on the spinning velocity. When the sample is accelerated to reach this velocity, the exceeding part of the deposited material is thrown away and then, during the uniform rotation, the thickness of the layer is set by the action of the viscous and centrifugal forces. This deposition procedure is called 'spin-coating'. After this process the sample was baked on a hot plate (120°C for 15 minutes) to completely evaporate the solvent and solidify the coating film. In a lift-off process the thickness of the resist has to be chosen considering the thickness of the metal that has to be deposited on the substrate. There's usually a good lift-off yield if the thickness of the resist results twice the thickness of the metal deposited on the substrate. It has to be noticed that in our fabrication procedure before the metalization the resist thickness was slightly reduced by the descum.

Step 2 and 3: EBL, development and descum

The lithographic system that we used to deliver into the resist the proper amount of electron in the final pattern is composed by a '*Zeiss ULTRA Plus*' SEM and a '*Raith Elphy Plus*' pattern generator.

In our procedure we set the accelerating voltage at 20 kV and then we placed the sample at 5mm from the end of the SEM column, performing electron imaging on a sample region far away from the final array position. In this early exposed region, we properly focused the electron beam on the resist surface and we adjusted its shape controlling the stigmators and the final aperture[1] position. Exploring other two points far away from the array region, we mapped the sample surface into a plane that was used to set by software the proper focus in every point of the sample during the exposition. Using these points we also mapped the coordinates

---

[1]For the lithography of the disks we used the aperture of 7.5 μm diameter, that allow the max resolution at a typical electron current the order of 25 pA.

of the CAD that represented the pattern to be exposed into the coordinate of the motorized stage. Set all the other exposition parameters, a computer controlled the remaining part of the process turning the beam on and off with a beam-blanker and deflecting it into the points of the sample that had to be exposed.

The most important of these other parameters is the amount of electrons that has to be delivered in the resist for unit of area (dose). For a certain set of exposure parameters, the result of the fabrication process depends also on the development and the descum procedures. We chose to develop the sample in the MIBK:IPA=1:3 ('*Allresist AR 600-56*') solution at room temperature for 2 minutes and to stop the development putting the sample for 30 seconds into 2-propanol. The descum was performed in a '*Gambetti Colibrì*' machine at an oxygen pressure of 0.45 mbar and using a radiofrequency power of 20 W. To find the proper dose associated to these development and descum procedures, we fabricated in a single exposition a series of array at different doses (dose array): the dose (260 $\mu C/cm^2$) that yielded the array of this series with the best disks shape is the dose that we employed in the samples fabrication.

To make easier the alignment of the array (whose typical dimension is 200 μm) in the time-resolved diffraction experiments, we exposed also some markers, four rectangles that are visible with the naked eye (their sides are 300 μm and 1 mm long)[2]. These markers were exposed in the same lithographic step of the disks, so they have the same properties compared to the disks (material, thickness, interface with the substrate).

Step 4: metalization and lift-off

The aluminum deposition was done using a thermal evaporator system, '*Kurt J. Lesker Nano38*'. The principle of the evaporation deposition is that the material

---

[2]To reduce the exposition time, we used in the exposition of these rectangle the largesst final aperture available that has a diameter of 120 μm, so an electron current the order of 5.5 nA.

evaporates from an hot source and condenses on the substrate. Evaporation takes place in a high-vacuum chamber so that vapors other than the source material are almost entirely removed before the beginning of the process, avoiding that the evaporated particles collide and react with an undesired background gas. In the high-vacuum chamber, the sample, covered by a movable shutter, was mounted in front of the tungsten crucible (also called boat) in which the material to deposit (the source) was placed. The chamber was pumped till a pressure of $1.4 \cdot 10^{-5}$ mbar was reached in it, then we run a current the order of tens of amperes in the crucible to heat the source to the aluminum melting point. The evaporation rate was measured by a quartz microbalance and when this rate was the order of 2 Å/s and stable, we rotated the shutter so that the evaporated material could reach the sample surface where an high fraction of atoms adhered and formed a film by condensation. When the material deposited had reached the desired thickness value, measured with the same quartz microbalance, we rotated the shutter to cover again the sample and reduced the current that was passing through the crucible slowly, to avoid any damage on the boat due to a thermal shock. The entire procedure was remote-controlled via software.

To solve the resist and remove the metal deposited on it, we placed the aluminum-coated sample in a beaker filled with hot (~ 50°C) acetone for 5 minutes. The acetone was also sprayed with a syringe on the sample surface to enhance the removal. If the resist was not washed out effectively in this way, we also put the sample (in beaker filled with acetone) in a sonicator. This procedure did not remove the aluminum disks deposited on the substrate because, due to the descum lithographic step, their adhesion was good. Finally we rinsed the sample in 2-propanol and quickly blew dry with the nitrogen gun.

4.2   Al-Si samples

The samples patterned on silicon substrate on which we also did measurements are listed in Table 4.1. All these silicon substrate were obtained cleaving a single Si(100) wafer having a thickness of 380 μm without removing the native oxide layer that was present on the silicon surface. The sides of the arrays were patterned nearly parallel to the Si(100) direction. In Figure 4.2 it is shown a SEM image of one of these samples at low magnification, and in Figure 4.3 the same sample region at higher magnification.

Sample name	diameter (nm)	periodicity (μm)	disks thickness
Al-Si h45 0	355 ± 5	1	47 ± 5
Al-Si h45	355 ± 5	1	45 ± 5
Al-Si h45 B	355 ± 5	1	45 ± 5
Al-Si h85	360 ± 10	1	85 ± 5
Al-Si h20	355 ± 5	1	25 ± 5

TABLE 4.1: Disks diameters as estimated by the SEM images. The thickness was checked by a stylus profilometer on the markers and with an AFM on the disks. On the sample '*Al-Si h45 0*' we did only the first preliminary measurements, while on the sample '*Al-Si h45 B*' we performed only test measurements that resulted in agreement with those on '*Al-Si h45*'. The data related to '*Al-Si h45 0*' and '*Al-Si h45 B*' are not reported in Chapter 5.
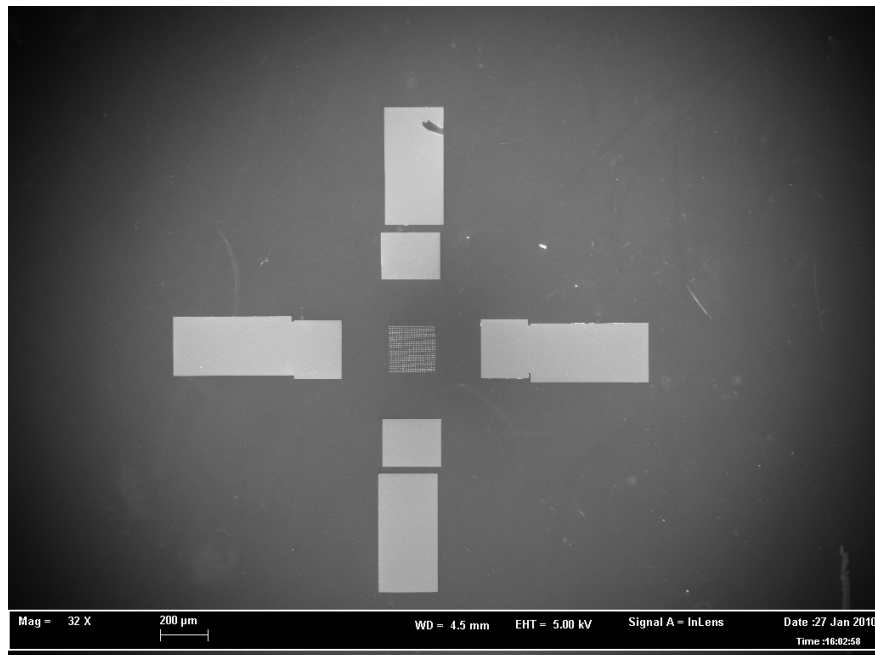
FIGURE 4.2: This is a SEM image of the sample at low magnification. The array is at center of the region between the markers.
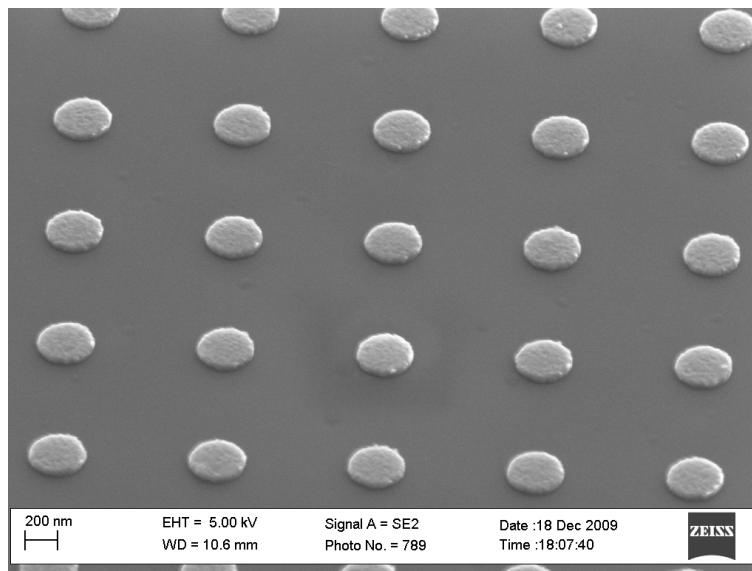

FIGURE 4.3: Tilted SEM image of the disks.

Chapter 5

Time-resolved optical investigation of hypersonic phononic crystals

In this chapter we illustrate the experimental setup and discuss the results of time-resolved optical diffraction measurements on '*Al-Si*' samples.

5.1 Time Resolved Diffraction experiment

The scheme of the experimental setup for time resolved diffraction measurements is shown in Fig. 5.1. The laser source is a Ti:Sapphire oscillator that generates pulses of 150 fs duration at a central wavelength of 790 nm. This cavity has been modified with a cavity dumper to make the repetition rate tunable over a broad range: we operated at 540 KHz.

The laser output is split into two beams of different intensity with a 30%-70% beamsplitter: the more intense pulse is used to pump the sample and the other is the probe. The pump beam passes through a mechanical chopper that modulates its intensity at a frequency $f = 3$ KHz. The lenght of the pump optical path can
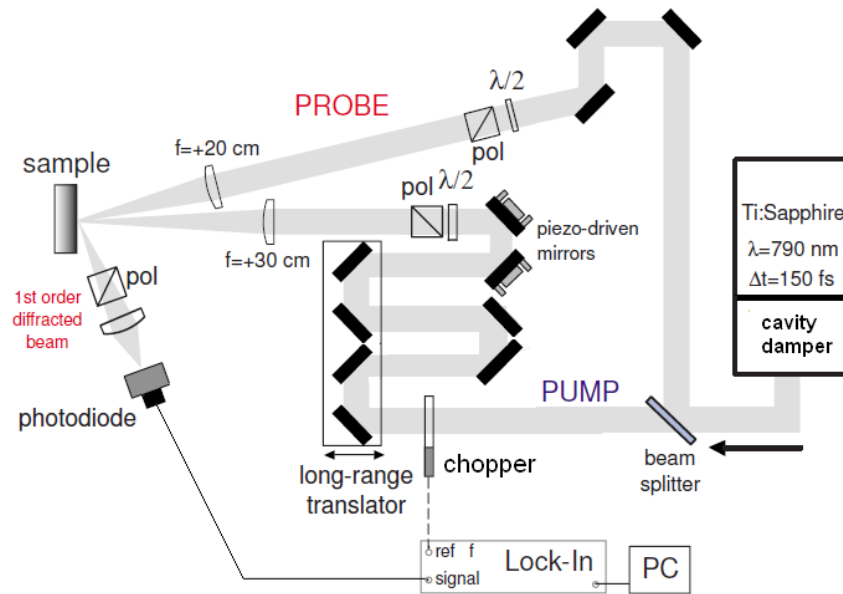
FIGURE 5.1: Scheme of the experimental setup used in the time-resolved diffraction measurements.

be varied by means of a long-range translation stage, whose travel is $\Delta x = 30$ cm. The beam undergoes a four passages reflection scheme over the translator, so it is possible to modify the delay between the arrival of the probe and the pump pulses on the sample within $\Delta t = c \cdot 4\Delta x \sim 4$ ns. Small imperfections in the motion of the translator introduce a systematic misalignment of the pump incident direction on the sample. To overcome this technical issue, the pump beam alignment is controlled by means of a feedback system, constituted by two motorized mirrors in cascade. With two telescopes the images of the pump on the last of these mirrors and in a point after it are taken: as the beam direction changes, also the imaged positions of these two points change and the motorized mirrors are driven to restore the correct alignment configuration. The pump beam intensity and polarization are selected by means of an attenuator composed of an half-wave plate coupled to a polarizer. Finally this beam is focused on the sample with a lens that has a focal lenght of 30 cm obtaining a pump spot diameter on the sample of 30 μm.

On the other optical arm, the probe path is designed to have a temporal overlap between the pump and probe pulses in proximity of the longest pump path configuration. The probe beam intensity and polarization are selected by means of an attenuator constituted by an half-wave plate coupled to a polarizer. The axis of this polarizer is perpendicular to the pump plane of polarization. Finally the probe is focused on the sample in spatial coincidence with the pump. The probe lens has a 20 cm focal length thus producing a 20 μm spot diameter and ensuring an uniformly excited probed region.

The spot of the first diffraction order of the probe in the plane of incidence is collected by means of a spherical mirror and passes through a polarizer parallel to the probe polarization to filter out the pump scattered light. Finally the diffracted signal is focused on a fast photodiode and analyzed with a lock-in amplifier technique. The signal component at the chopper modulating frequency f corresponds to the pump-induced intensity variation. This technique is particularly suitable to increase the signal to noise ratio and to detect relative intensity variation of the signal $\Delta I/I \sim 10^{-6}$. The higher is the modulating frequency, less noisy will be the measurement. The entire measurement procedure is remote-controlled using a customized LabView acquisition program.

5.2   Decoupling the thermal and mechanical dynamics tuning the filling fraction

The measurements on the '*Al-Si h85*', '*Al-Si h45*' and '*Al-Si h20*' samples are reported in Fig. 5.2 and the relevant fit parameters of the data interpolation are summarized in Table 5.1.
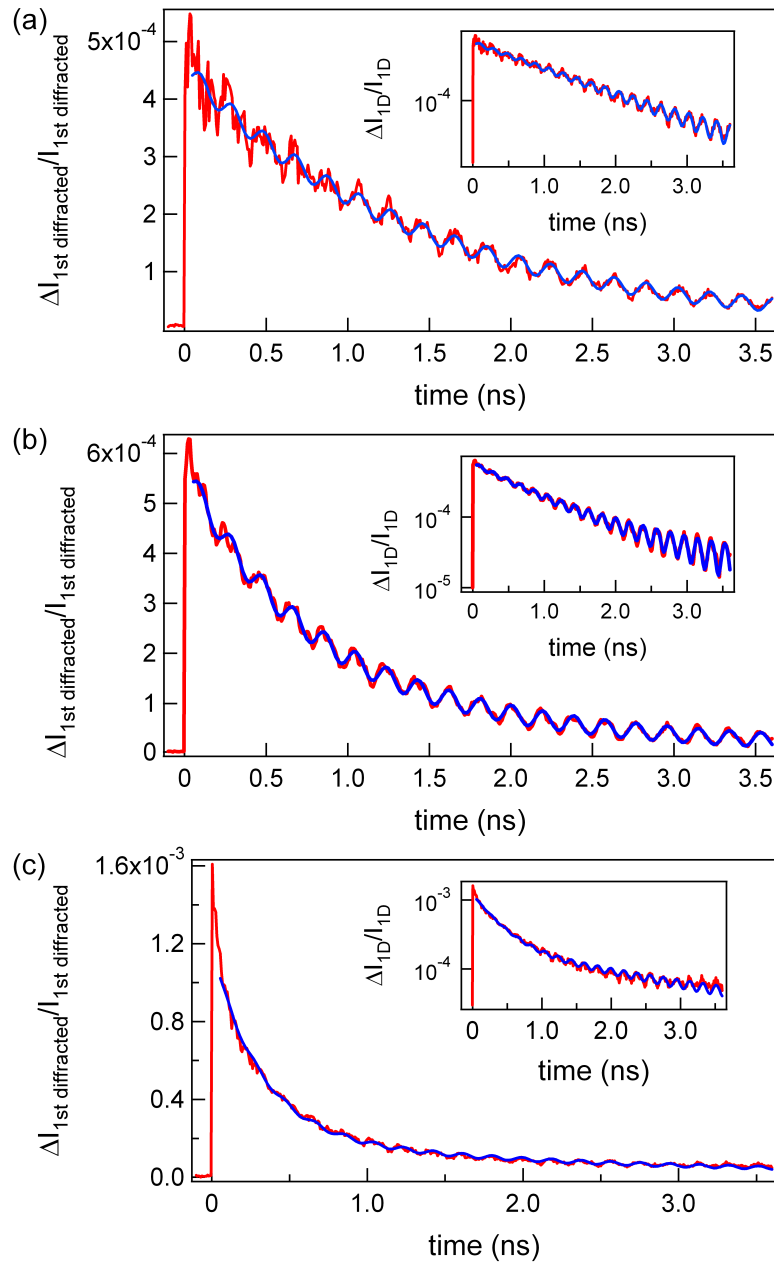
FIGURE 5.2: These are the plots of the measurements on '*Al-Si h85*' in panel (a), '*Al-Si h45*' in panel (b) and '*Al-Si h20*' in panel (c). The measurements are performed with a pump fluence of 2.8 J/m^2 and a probe fluence of 1.2 J/m^2. The red lines are the data, while the blue ones are the fit. In the insets the graphs have $\Delta I_{1D}/I_{1D}$ in logarithmic scale to better appreciate if the thermal dynamics can be described with single or double exponential decay.

Sample name	τ_{SAW} (ns)	ν_{SAW} (GHz)	$\tau_{th,1}$ (ps)	$\tau_{th,2}$ (ns)
Al-Si h85	9 ± 5	5.123 ± 0.004	1450 ± 30	
Al-Si h45	7 ± 1	5.238 ± 0.002	660 ± 130	1.6 ± 0.9
Al-Si h20	9	5.26 ± 0.01	310 ± 10	2.1 ± 0.5

TABLE 5.1: The fit parameters obtained fitting the data in Fig. 5.2 using the fit function $y_0 + A_1 e^{-t/\tau_{th,1}} + A_2 e^{-t/\tau_{th,2}} - B e^{-t/\tau_{SAW}} \cos(2\pi\nu_{SAW}t)$. In the case of '*Al-Si h20*' there are convergence problem if τ_{SAW} is kept as a running parameter so we fix it at 9 ns. In the case of '*Al-Si h85*' using the two exponential decays for the thermal part we obtained two equal decay times, so we dropped one of them.

An oscillation at 5 GHz emerged in every measurement and this can be attributed to the cos-like pseudo-SAW eigenmode of the phononic crystal with reduced vector $k_x = 0$ and $n = 1$ (see Section 2.1). It is evident from these data that we succeeded in decoupling the thermal and mechanical time scales by choosing the proper filling fraction, making the pseudo-SAW lifetime ($\tau_{SAW} > 7$ ns) longer than the thermal relaxation time ($\tau_{th} \lesssim 1.5$ ns). The pseudo-SAW lifetime estimation was not very precise, but without doubts it was greater than the experimental temporal window (~ 3.5 ns) in which we followed the fast thermal dynamics.

In the case of '*Al-Si h85*' the thermal dynamics is described by a single exponential, as predicted by the model in Section 2.2. Evaluating Eq. 2.4, using the τ_{th} extracted from this data set and the aluminum material properties (reported in note [16]), we find that the thermal resistance of the aluminum-silicon interface is $(7.0 \pm 0.4) \cdot 10^{-9}$ m^{2}K/W, in agreement with the values reported in Ref. [23].

For '*Al-Si h45*' and '*Al-Si h20*' a single thermal exponential decay is not suitable, even if the Biot number is $B \sim 0.05$. In the case of '*Al-Si h45*' the thermal dynamics is well described by a double exponential decay. In the case of '*Al-Si h20*' a double exponential interpolated well the first nanosecond but not the subsequent dynamics, so the parameters of this fit are only useful to have an estimation

Sample name	$\tau_{th,1}$ (ps)	$\tau_{th,2}$ (ns)
Al-Si h85	1300 ± 100	
Al-Si h45	560 ± 30	3 ± 2
Al-Si h20	280 ± 10	1.6 ± 0.4

TABLE 5.2: Fit parameters obtained from the data on the markers. The oscillating term of the fit function for the disks data showed in the caption of Table 5.1 is dropped.

of $\tau_{th,1}$.

The same thermal behavior was observed also in the measurements on the alignment markers (see Table 5.2). Due to their millimetric dimensions, the marker can be considered as a film of the same thickness and material properties of the nanodisks (see Section 4.1). The fact that the thermal dynamics observed on the marker and on the nanodisks was the same validates the approximation of the disk with a film done in the model described in Section 2.2. Two possible explanations emerge for the discrepancy between our model and the data on '*Al-Si h45*' and '*Al-Si h20*':

1. the heat flux cannot be described with the Fourier law;

2. the substrate cannot be considered at a uniform and constant temperature throughout the thermalization process [7].

Comparing our results with the ones reported in Ref. [24], we conclude that the heat transport in our samples can be regarded Fourier-like. Hence we consider that the thermal dynamics occurs into the following two steps. The isothermal nanodisk 'feels' a substrate constant temperature and it thermalizes with it within $\tau_{th,1}$, as calculated on the basis of the isothermal disk model (see section 2.2). On the longer time scale $\tau_{th,2}$ the disk and the Si substrate portion in close proximity to the disk-Si interface jointly thermalize with the rest of the Si substrate. The

fast decay time $\tau_{th,1}$ scaled linearly with the disks thickness, as shown in Table 5.1 and in agreement with the coarse analytical model addressed in Section 2.2. We pin-point that the slow decay time $\tau_{th,2}$ on '*Al-Si h45*' was not well estimated by the fit because it was close to the maximum delay that we could explore ($\sim$ 3.5 ns).

Summarizing, we were able to decouple the thermal and mechanical time scales by tailoring the filling fraction and by an appropriate choice of the metal. The thermal decay time $\tau_{th,1}$ scaled linearly with the disks thickness, as expected on the basis of an unsophisticated analytical model.

5.3   Quenching the SAW via a PDMS coating

We performed the time-resolved optical diffraction experiment on the same samples of the previous section also when the phononic crystals were coated with a 1.4 mm thick PDMS overlayer, and these measurements are reported in Fig. 5.3. We prepared a PDMS slab of this thickness by dropping 10 mg of PDMS oil on a silicon wafer and polymerizing it; the employed overlayers were cut from this slab and attached on the samples exploiting the conformal bonding property of PDMS.

To better understand the role of the mass loading effect of the overlayer, we investigated also the case in which the PDMS overlayer was directly deposited on the sample by spin-coating. In this way we had an overlayer of a lower thickness: we did not measure this thickness, but we estimated it to be in the order of tens of microns. The mass loaded by the spin-coated overlayer on the Si substrate surface hence is significantly different from the mass loaded by other PDMS overlayer. The fit parameters of these measurements are summarized in Tables 5.3 and 5.4.
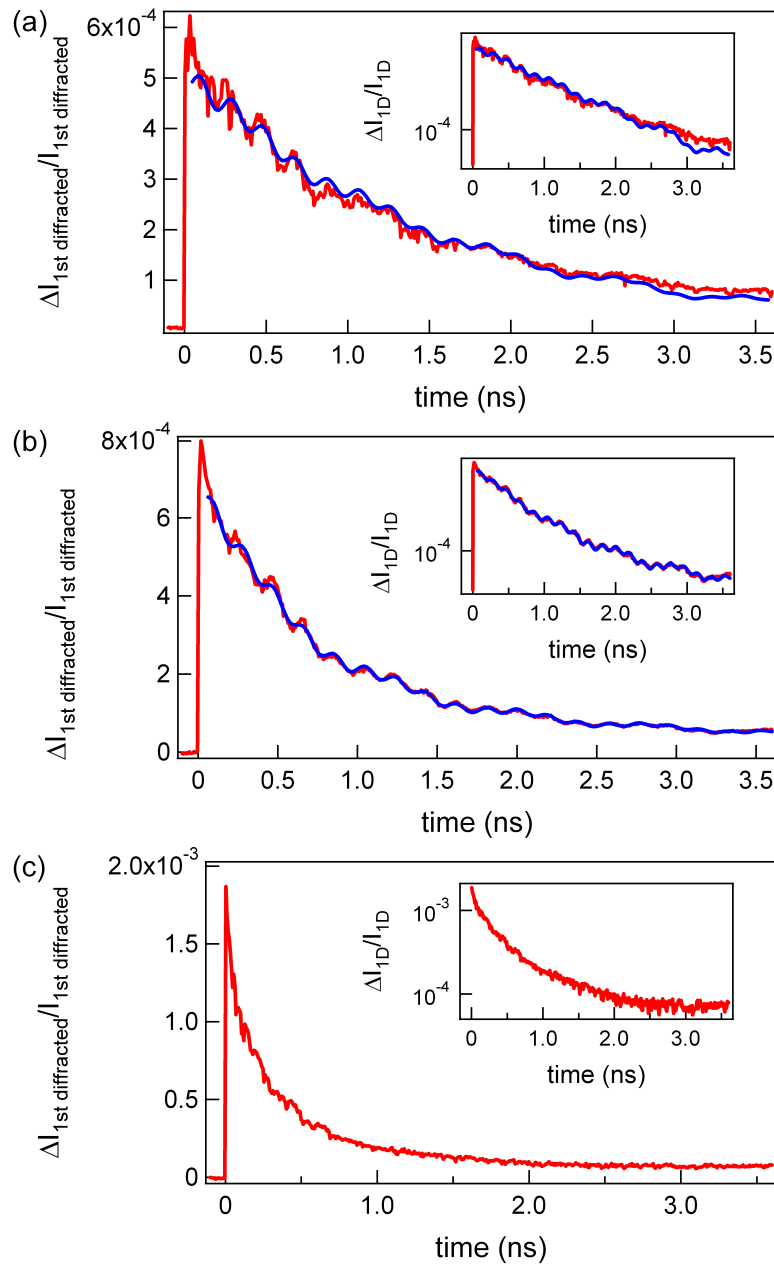
FIGURE 5.3: These are the plots of the measurements on '*Al-Si h85*', in panel (a), '*Al-Si h45*', in panel (b), and '*Al-Si h20*', in panel (c), when we cover their surface with a PDMS overlayer of 1.4 mm thickness. The measurements are performed with a pump fluence of 2.8 J/m^2 and a probe fluence of 1.2 J/m^2. The red lines are the data, while the blue ones are the fit. In the insets the graphs have $\Delta I_{1D}/I_{1D}$ in logarithmic scale to better appreciate if the thermal dynamics can be described with single or double exponential decay.

	Al-Si h85		Al-Si h45	
PDMS	1.4mm slab	spin-coated	1.4mm slab	spin-coated
ν_{SAW} (GHz)	5.12 ± 0.02	5.10 ± 0.01	5.24 ± 0.01	5.23 ± 0.01
τ_{SAW} (ns)	1.3 ± 0.3	1.2 ± 0.2	1.4 ± 0.1	1.4 ± 0.2
ν_{PDMS} (GHz)	1.30 ± 0.01	1.28 ± 0.01	1.22 ± 0.01	1.18 ± 0.01
τ_{PDMS} (ns)	8 ± 7	5 ± 3	1.9 ± 0.2	3 ± 1

TABLE 5.3: Parameters obtained by fitting the data reported in Fig. 5.3. Attention is here drawn on the acoustic dynamics only. With respect to the uncoated case, we add in the fit function a second oscillating term $-B_2 e^{-t/\tau_{PDMS}} \cos(2\pi\nu_{PDMS}t)$ to account for the oscillation at 1 GHz.

We had that the pseudo-SAW lifetime ($\tau_{SAW} \sim 7$ ns in the uncoated case) was reduced to $\tau_{SAW} \sim 1.5$ ns by the presence of the overlayer. Since the thick and the thin coatings led to similar results, we conclude that the mass loading effect has a negligible role in the SAW damping process.

Comparing the Fourier transform of the measurements with and without PDMS (see Fig. 5.4), it has to be noticed that a new peak at 1.2 GHz appeared when the PDMS overlayer was deposited. This frequency is attributed to a longitudinal wave of 1 μm wavelength in the PDMS, in fact the velocity of longitudinal wave in PDMS varies from 900 m/s to 1500 m/s depending on the cross-link density [25, 26]. Further investigations are needed to properly explain the excitation of this wave and its relation with the SAW damping. A tentative scenario is that this wave is excited with the same mechanism by which the SAW is launched and that the silicon surface can slide at the Si-PDMS interface, in this way losing mechanical energy into heat. The longitudinal wave in PDMS is not so much affected by friction because, being a bulk wave, much of its mechanical energy content is within the PDMS bulk. We performed the acoustics analysis on '*Al-Si h85*' and '*Al-Si h45*'. Unfortunately, we could not perform the same analysis on '*Al-Si h20*': the
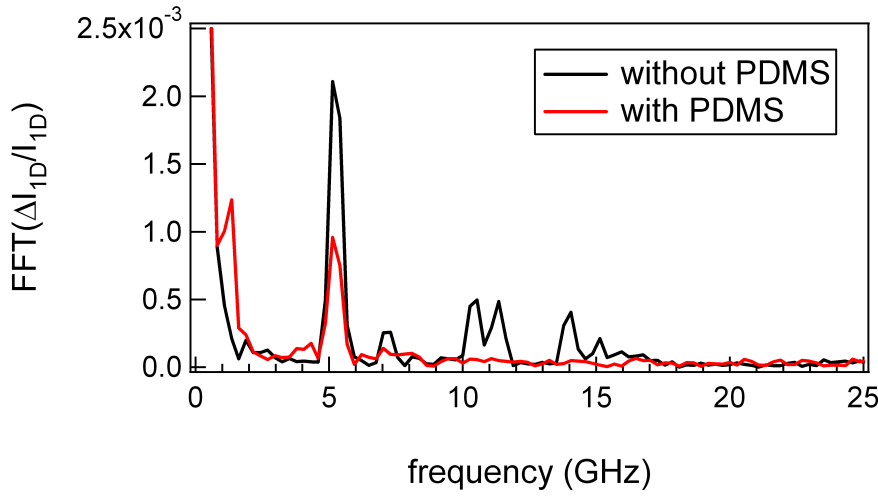
FIGURE 5.4: These are the magnitudes of the Fourier transform of the data on '*Al-Si h45*' with 1.4 mm thick PDMS overlayer (red line) and without the coating (black line).

oscillations in this case were only detectable within the first nanosecond, without a significant signature in the Fourier transform of the signal.

A last issue has to be addressed: an useful coating for studying the heat transfer should not affect the thermal problem (see Section 3.2.2). In the '*Al-Si h45*' case the fast decay time did not change when we deposited the PDMS on the sample surface. In the case of '*Al-Si h85*' the single thermal exponential fit the data not so well as in the uncoated case. There are at least two possibilities for explaining this discrepancy.

1. The single exponential decay is the proper interpretation of the thermal dynamics of the sample, but the interpolation when the PDMS overlayer was added was not as good as in the uncoated case because $\tau_{SAW} \sim \tau_{th}$.

2. The single exponential decay time fit well the uncoated case, but not in the PDMS coated one because the PDMS overlayer altered the thermal problem. Nevertheless, if this is the case it has to be understood why this seems not to be the case in the '*Al-Si h45*' fast dynamics.

Sample name	PDMS coating	$\tau_{th,1}$ (ps)	$\tau_{th,2}$ (ns)
Al-Si h85	1.4mm slab	1520 ± 20	
	spin-coated	1350 ± 30	
Al-Si h45	1.4mm slab	640 ± 40	4 ± 8
	spin-coated	570 ± 40	3 ± 3
on the marker	spin-coated	550 ± 125	6 ± 30

TABLE 5.4: Parameters obtained by fitting the data reported in Fig. 5.3. Attention is here drawn on the thermal dynamics only. With respect to the uncoated case, we add in the fit function a second oscillating term $-B_2 e^{-t/\tau_{PDMS}} \cos(2\pi\nu_{PDMS}t)$ to account for the oscillation at 1 GHz.

The double exponential decay fit on the '*Al-Si h20*' was used in the uncoated case to give an estimate of $\tau_{th,1}$, but it did not fit well the dynamics on the entire range. With the PDMS coating there is a problem in the fit of the first nanosecond because we could see the oscillation but it is difficult to fit them, so it is not possible to compare the thermal behavior of this sample with and without the overlayer.

In conclusion, we were able to quench the SAW by means of a PDMS overlayer deposited on the surface-based phononic crystal without affecting the thermal relaxation dynamics of the composite systems under investigation.

Chapter 6

Conclusions and perspectives

In this thesis, we have identified two strategies to decouple the thermal and mechanical time scales of surface-based phononic crystals in time-resolved optical diffraction measurements.

The first is based on choosing the proper geometry of the phononic crystal to make the lifetime of the fundamental $k_x = 0$ $n = 1$ pseudo-SAW mode greater than the thermal decay time. Following this consideration we fabricated phononic crystals in which an ordered array of aluminum nanodisks with a low filling fraction geometry (350 nm disks diameter, 1 μm array periodicity) was deposited on the surface of a silicon substrate. In the time-resolved optical diffraction experiments we found that with this sample geometry we succeeded in decoupling the acoustical and thermal problem. We realized three samples with different disks thicknesses (85nm, 45 nm and 20nm) to investigate how the thermal relaxation dynamics changes with this parameter. We conclude that the model described in Section 2.2 is suited for the description of the thermal relaxation for the 85 nm disk thickness. For the other two configurations further investigation is needed to understand the discrepancy with the model.

The second strategy is to coat the sample with a damping overlayer. We adopted two kinds of polydimethilsiloxane (PDMS) overlayers: we investigated

both the case in which a 1.4 mm thick slab is attached on the sample and the case in which PDMS is directly spin-coated on the sample surface. In both cases we found that the SAW lifetime was reduced from $\sim$ 7 ns to $\sim$ 1.5 ns. Because the same lifetime was measured with the thin (spin-coated) and the thick (1.4 mm overlayer) PDMS overlayer, we conclude that the mass loading effect is not the main reason for the Si pseudo-SAW quenching process. We also detected a 1.2 GHz oscillation, attributed to a the longitudinal bulk wave in PDMS with wavelength 1 μm. Further investigations are needed to single out the excitation mechanism for this wave and how it is related to the Si pseudo-SAW quenching process. Comparing the measurement with and without PDMS on the sample with a 45 nm disks thickness it's possible to conclude that the PDMS overlayer does not affect the thermal problem.

Appendix A

The case of the glass substrate

In this appendix we analyze the fabrication process of surface-based hypersonic phononic crystals on a glass substrate (Section A.1) and the results of preliminary measurements on these samples (Section A.3).

A.1   Electron beam lithography on glass

When electron beam lithography is performed on an electrical insulating substrate (like glass), it is necessary to face the charging effect. In a conductive sample the electrons delivered in the system during the exposition quickly follow a path to ground because the substrate is kept in electrical contact with the metallic sample holder (that is grounded) by a metallic clamp or a conductive scotch. When the substrate is an electrical insulator, the embedded electrons take a much longer time to move to ground and during the exposition the sample results negatively charged. The range of the low-energy secondary electrons that contribute to the charging is not a fixed number so the deflection that they induce in the beam direction near the sample surface is not reproducible and it's difficult to compensate it in a valid manner via software. The charging problem also afflict the SEM imaging introducing noise and lowering the contrast so it's no more possible to
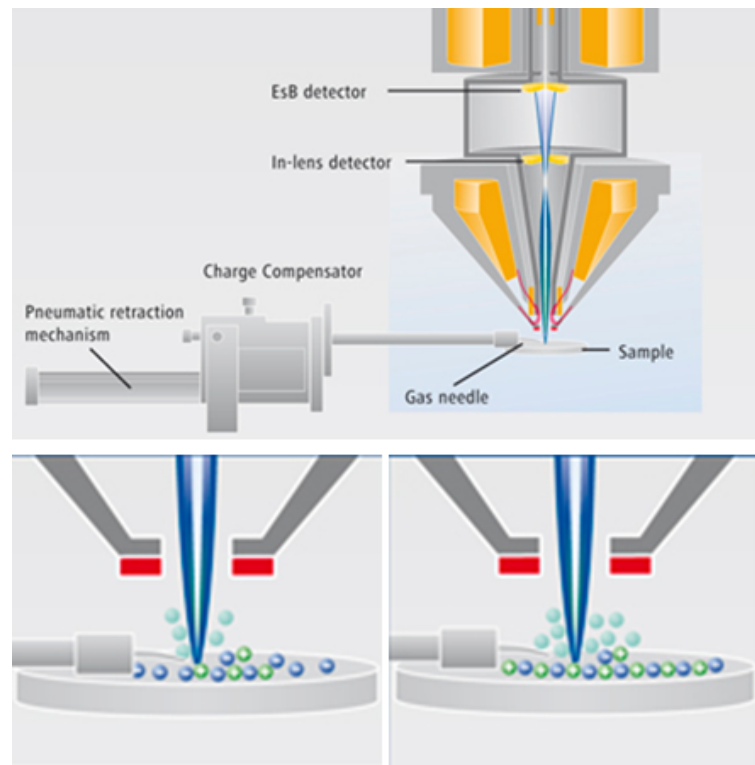
41

FIGURE A.1: Secondary Electrons (SE) and Back Scattered Electrons (BSE) emitted from the sample surface ionize the gas molecules. As the resulting positive ions (dark green) hit the sample surface it is neutralized. Full imaging capabilities are thus enabled.

focus the beam finely on the surface.

The '*Zeiss ULTRA Plus*' SEM has a new special feature, called charge compensator, to make possible the imaging on a small area of non-conductive samples without a special preparation (like coating it with a conductive layer). The charge compensator is a small capillary that inject nitrogen gas in the SEM field of view: the molecules of the gas are ionized by secondary and backscattered electrons and these positive ions hit the substrate surface neutralizing it (see Fig. A.1). In this way full imaging capabilities are recovered even on an insulating sample. We adopted for the first time this feature present on '*ULTRA Plus*' to solve the charging problem also in a lithographic process. This technique could allow to

obtain a better disks shape and a higher reproducibility of the deposited nanos-
tructure compared with others techniques used to solve this problem (for example,
an etching process on a metallic film or a coating of the resist with a temporary
conductive layer).

Like in the exposition of silicon substrate, we performed the lithography using
an accelerating voltage of 20 kV, but to be close to the charge compensator the
working distance was lower (~ 3.3 mm) and, due to the nitrogen flow, the pressure
in the SEM sample chamber was greater ($\sim 4 \cdot 10^{-3}$ mbar). All the other recipes
described in Chap. 4 were adopted also in the fabrication of samples based on glass
substrate, except the resist deposition that was changed to ensure a better lift-off
yield also in the case of ~ 85 nm thick disks. To obtain a resist layer thicker than
the one used for the patterning of silicon-based samples, we employed the '*Allresist
AR-P 679.04*' PMMA resist solution and deposited it spinning the sample at 6000
rpm. To enhance the resist adhesion on the substrate, the glass surface was also
previously cleaned by an oxygen plasma treatment. By a dose array on the glass
substrate, we found that the optimal dose for this procedure was 250 μC/cm^2.

To appreciate the charge compensator effects, in the dose array we exposed
also a series of array turning off the gas injection (see Fig. A.2). From SEM im-
ages (done with the charge compensator on), we found that the disks shape did
not change too much with or without the charge compensator, while the lattice
structure resulted to be seriously distorted if the charge compensator was turned
off. It was possible to find a small distortion at the edges of the patterned lattice
even when the charge compensator was turned on and this is due to the finite
size of the neutralized area. We have found that patterning an array of 100 μm
side length, we could obtain no distortions, but this result was very sensitive on
the positioning of the charge compensator in respect to the exposed area, so the
maximum area that could be easily exposed without distortion using the charge
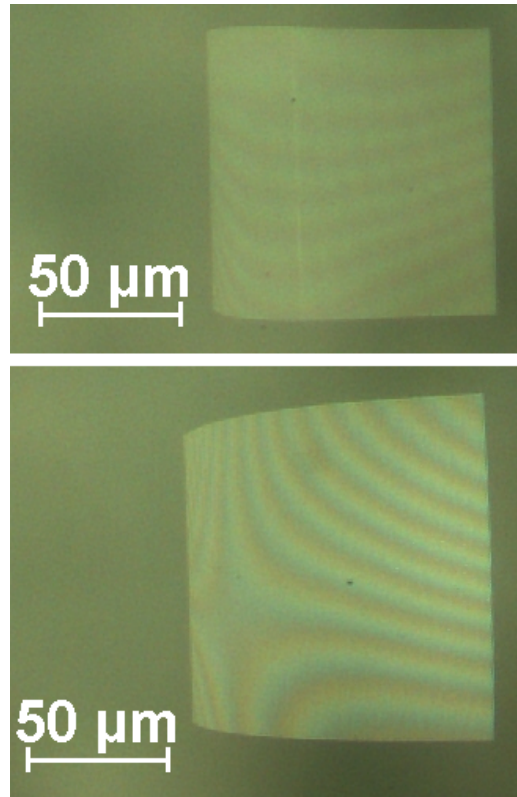compensator was the order of 100 μm$\times$ 100 μm.

FIGURE A.2: Top panel: optical microscope of an array exposed with the charge compensator-assisted EBL. Bottom panel: an array exposed on the same sample with the same parameters but with the charge compensator turned off.

A.2   Al-Glass samples

We fabricated three samples on the glass substrate. In these samples the square array of nanodisks has lines of 99 disks arranged with a periodicity of 1 μm. In the samples '*Al-Glass h40*' and '*Al-Glass h40B*', the disks thickness is the same and equal to 39 nm, while disks diameter is different: in '*Al-Glass h40*' the disks diameter is (360 ± 5) nm, while in the other is (420 ± 5) nm. In the third sample, called '*Al-Glass h80*', the disks diameter is (360 ± 5) nm and the disk thickness is 81 nm. These thicknesses were measured with a stylus profilometer on a film that was evaporated on a glass substrate placed next to the patterned samples in the

evaporation chamber. The disks diameter was estimated by SEM imaging.

We can see in Fig. A.3 the global structure of the arrays. In '*Al-Glass h40*' there's only a very small defect and this is the best result that we have obtained exposing an area of 100 μm ×100 μm. This kind of defects at one edge of the patterned area were not a problem in our experiments because the laser pumped area had a diameter of 30 μm and the properties of the system were probed within the same region and so there was a large regular area available on these patterned samples. In Fig. A.4 there is shown an high resolution SEM image of the disks fabricated by the charge compensator-assisted EBL technique.
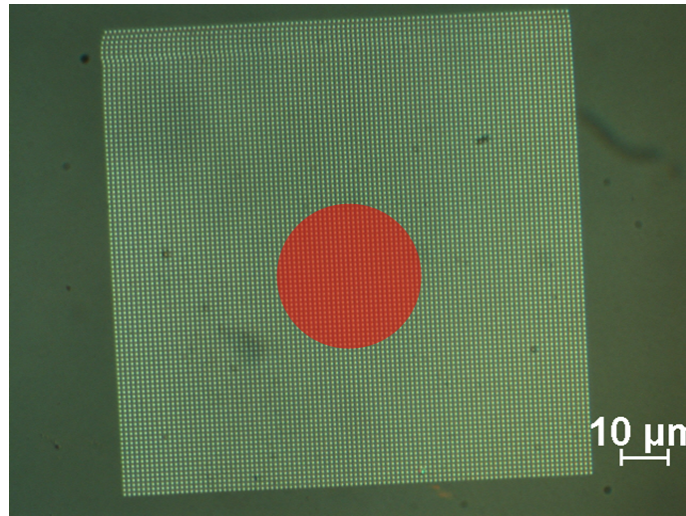
FIGURE A.3: This image of the sample '*Al-Glass h40*' was taken using an optical microscope with a 100× objective lens. The periodicity of the array results broken only near the top edge few micrometers, but a large area remains available for the pump and probe technique. For a comparison we draw a circle with the same diameter of our laser spot.
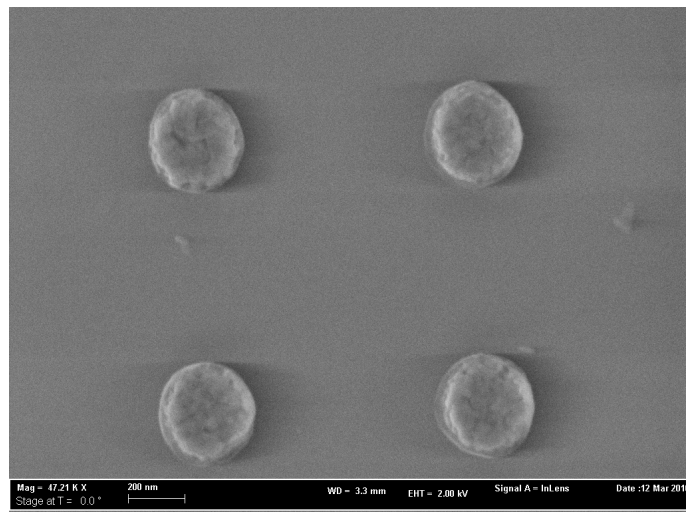

FIGURE A.4: SEM images of the disks patterned on the sample '*Al-Glass h80*'. We can see that with the use of the charge compensator it's possible to perform an high magnification SEM imaging on insulator without the typical problems related to the electron charging.

Sample name	1st diffracted position	τ^{th} (ns)
Al-Glass h40	Reflection	4.7 ± 0.5
Al-Glass h40	Trasmission	4.1 ± 0.4
Al-Glass h40B	Reflection	4.6 ± 0.6
Al-Glass h40B (PDMS)	Reflection	3.8 ± 0.6
Al-Glass h80	Reflection	8 ± 2

TABLE A.1: The thermal relaxation times obtained fitting the data plotted in Fig. A.5 with a single exponential decay function are here reported.

A.3   Measurements

In the measurements performed on the '*Al-Glass*' samples, reported in Fig. A.5, no oscillations emerged in contrast with the behavior predicted by the model in section 2.1, but it has to be noticed that the signal to noise ratio in these measurements was worse than in the experiments on '*Al-Si*' samples. The data have a single exponential decay with a thermal relaxation time of the order of our experimental temporal window or greater (see Table A.1), so we point out that the maximum explorable delay has to be increased to have a more accurate estimation. Comparing the results on '*Al-Glass h40*' and '*Al-Glass h40B*', the thermal decay appeared to be independent from the disks diameter, so there was no effect due to the lateral confinement as expected for this substrate [24]. Comparing the thermal decay of '*Al-Glass h40*' and '*Al-Glass h80*', we observed that τ_{th} was proportional to the disks height, even though the estimation of τ_{th} in '*Al-Glass h80*' was not precise. Taking this information into account, we conclude that the thermal relaxation of these samples is well described by the model implemented in Section 2.2.

We investigated also the case in which the '*Al-Glass h40B*' sample was coated with a 1.4 mm thick PDMS overlayer. In the '*Al-Si*' samples, when the PDMS coating was deposited, it appeared an oscillation at 1.2 GHz, that we associated
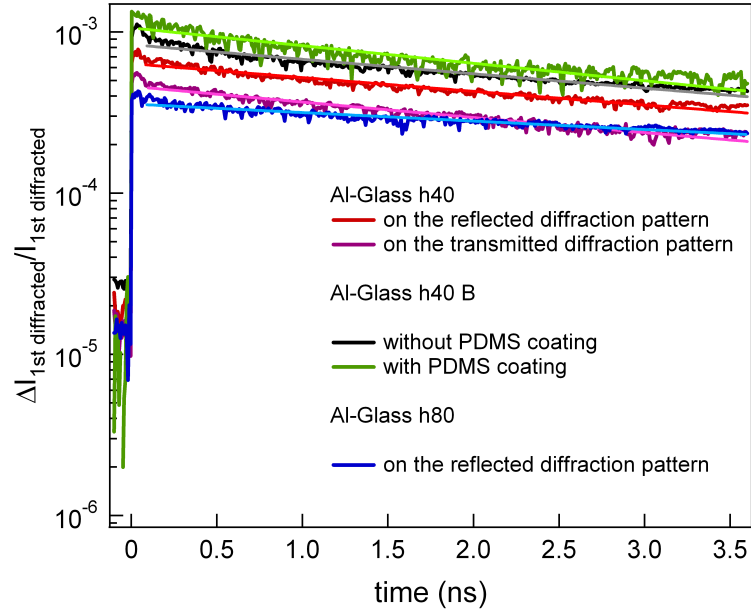
FIGURE A.5: Plots of the measurements on '*Al-Glass*' sample. The left axis in the logarithmic scale to appreciate the single exponential behavior

to the PDMS longitudinal bulk wave of 1 μm wavelength. No oscillations were detectable in the '*Al-Glass*' uncoated case, hence if we coated the sample and we measured a 1.2 GHz oscillation, we could conclude that the excitation of this wave induced by the stress directly applied on the rubber by the disks expansion is significant. We did not detect this oscillation in the measurement on '*Al-Glass h40B*' coated sample. This fact does not prove that the PDMS wave observed in the '*Al-Si*' case was not directly excited by the disks, because we are not sure that the 1.2 GHz oscillations were not hidden by the noise of a single measurement, as for the glass oscillation. From this measurement we observed that PDMS did not affect the thermal problem, but it seems rash to draw a definite conclusion on this point due to the fact the thermal decay time in this sample was of the order of our experimental temporal window.

We also performed measurements on the transmitted diffraction pattern and checked that there was no difference in the τ_{th} estimation.

Bibliography

[1] M. Cecchini, V. Piazza, F. Beltram, D. G. Gevaux, M. B. Ward, A. J. Shields, H. E. Beere, and D. A. Ritchie, Appl. Phys. Lett. **86**, 241107 (2005).

[2] M. Cecchini, V. Piazza, G. D. Simoni, F. Beltram, H. E. Beere, and D. A. Ritchie, Appl. Phys. Lett. **88**, 212101 (2006).

[3] J. Rudolph, R. Hey, and P. V. Santos, Phys. Rev. Lett. **99**, 047602 (2007).

[4] M. M. de Lima, R. Hey, P. V. Santos, and A. Cantarero, Phys. Rev. Lett. **94**, 126805 (2005).

[5] M. M. de Lima, M. van der Poel, P. V. Santos, and J. M. Hvam, Phys. Rev. Lett. **97**, 045501 (2006).

[6] W. C. Fon, K. C. Schwab, J. M. Worlock, and M. L. Roukes, Nano Lett. **5**, 1968 (2005).

[7] F. Banfi, F. Pressacco, B. Revaz, C. Giannetti, D. Nardi, G. Ferrini, and F. Parmigiani, Phys. Rev. B **81**, 155426 (2010).

[8] C. Giannetti *et al.*, Phys. Rev. B **76**, 125413 (2007).

[9] D. Nardi, *Thermomechanics of hypersonic phononic crystals*, PhD thesis, Università degli Studi di Milano (2010).

[10] L. D. Landau and E. M. Lifshitz, *Theory of Elasticity* (Butterworth-Heinemann, Oxford, 1986).

[11] A. Cleland, *Foundations of Nanomechanics* (Springer, Berlin, 2003).

[12] A. A. Maznev and O. B. Wright, J. Appl. Phys. **105**, 123530 (2009).

[13] D. Nardi, F. Banfi, C. Giannetti, B. Revaz, G. Ferrini, and F. Parmigiani, Phys. Rev. B **80**, 104119 (2009).

[14] C. Kittel, *Introduction to solid states physics, 7th ed.* (John Wiley and Sons, New York, 1996).

[15] B. Auld, *Acoustic Fields and Waves in Solids, Vol.II* (Krieger Publ., Malabar, FL, 1990).

[16] It has to be considered that in our experiments the pump laser pulse has an energy of $\sim$ 15 nJ and a spot diameter of $\sim$ 30 μm. The aluminum disks have a diameter of $\sim$ 350 nm and are arranged on a square lattice of 1 μm of periodicity. Different samples have different disks thickness, and this is in the range from 20 nm to 85 nm. Aluminum has a Young Modulus of 71 GPa, a density of 2700 Kg/m^3, a specific heat capacity for unit of mass of 897 J/(KgK), a coefficient of linear expansion of $23.1 \cdot 10^{-6}$ K^{-1}. The reflectance of aluminum at 800 nm wavelength in normal incidence is $R = 0.868$. The aluminum material properties are taken from [17].

[17] M. Weber, *Handbook of optical materials* (CRC Press, Boca Raton, 2003).

[18] F. Pressaco, *Studio di fattibilità per una tecnica completamente ottica per misure nanocalorimetriche*, Master thesis, Università degli Studi di Trieste (2008).

[19] M. N. Özişik, *Heat Conduction, II Ed.* (Wiley-Interscience, Malabar, FL, 1993).

[20] M. E. Siemens, Q. Li, M. M. Murnane, H. C. Kapteyn, R. Yang, E. H. Anderson, and K. A. Nelson, Appl. Phys. Lett. **94**, 093103 (2009).

[21] C. Giannetti, F. Banfi, D. Nardi, G. Ferrini, and F. Parmigiani, IEEE Photonics Journal **1**, 21 (2009).

[22] Y. S. Shin, K. Cho, S. H. Lim, S. Chung, S.-J. Park, C. Chung, D.-C. Han, and J. K. Chang, J. Micromech. Microeng. **13**, 768 (2003).

[23] Davies and Associates, *14ASM Metal Handbook, 10th ed.* (ASM International, Metals Park, 1996).

[24] M. E. Siemens, Q. Li, R. Yang, , K. A. Nelson, E. H. Anderson, M. M. Murnane, and H. C. Kapteyn, Nature Materials **9**, 26 (2010).

[25] J. Mark, *Physical properties of polymers handbook, 2nd ed.* (Springer, Berlin, 2007).

[26] S. Kondo and T. Igarashi, J. Appl. Phys. **51**, 1514 (1979).